Geophysical and Astrophysical Fluid Dynamics
Vol. 00, No. 00, 00 Month 2018, 1–14

GAFD Special issue on "Physics and Algorithms of the Pencil Code"

The timestep constraint in solving the gravitational wave equations sourced by hydromagnetic turbulence

A. ROPER POL[a,b], A. BRANDENBURG[b,c,d,e], T. KAHNIASHVILI[e,f,g], A. KOSOWSKY[h], & S. MANDAL[e]

[a]Department of Aerospace Engineering Sciences, University of Colorado, Boulder, CO 80303, USA
[b]Laboratory for Atmospheric and Space Physics, University of Colorado, Boulder, CO 80303, USA
[c]JILA and Department of Astrophysical and Planetary Sciences, University of Colorado, Boulder, CO 80303, USA
[d]NORDITA, KTH Royal Institute of Technology and Stockholm University, and Department of Astronomy, Stockholm University, SE-10691 Stockholm, Sweden
[e]McWilliams Center for Cosmology and Department of Physics, Carnegie Mellon University, 5000 Forbes Ave, Pittsburgh, PA 15213, USA
[f]Department of Physics, Laurentian University, Ramsey Lake Road, Sudbury, ON P3E 2C, Canada
[g]Abastumani Astrophysical Observatory, Ilia State University, 3-5 Cholokashvili St., 0194 Tbilisi, Georgia
[h]Department of Physics and Astronomy, University of Pittsburgh, and Pittsburgh Particle Physics, Astrophysics, and Cosmology Center (PITT PACC), Pittsburgh PA 15260

(*July 17, 2018, Revision: 1.59*)

Hydromagnetic turbulence produced during phase transitions in the early universe can be a powerful source of stochastic gravitational waves (GWs). GWs can be modeled by the linearized spatial part of the Einstein equations sourced by the Reynolds and Maxwell stresses. We have implemented a GW solver into the Pencil Code, which uses a third order timestep and sixth order finite differences. We study the appearance of a numerical degradation of the GW amplitude at the highest wavenumbers, which depends on the length of the timestep—even when the Courant-Friedrichs-Lewy condition is ten times below the stability limit. This degradation leads to a numerical error, which is found to scale with the third power of the timestep. A similar degradation is not seen in the magnetic and velocity fields. Yet, we argue that such degradation could also occur in those fields, but it is being masked by the forward cascade of energy, which populates all higher wavenumbers in a timestep-independent fashion. A similar process is not possible for the GWs, because their evolution equations are linear.

Keywords: Gravitational waves; Early Universe; Aeroacoustics; Turbulence

1. Introduction

Wave equations coupled to the fluid equations appear in at least two different contexts. The Lighthill equation in aeroacoustics is one such example (Lighthill 1952, 1954), and the linearized gravitational wave (GW) equation is another (e.g. Grishchuk 1974, Deryagin et al. 1986). The former example is important not only in aviation, where the Lighthill equation is used to quantify the sound production from jet engines, but it is also relevant to stars with outer convection zones, where sound waves from the outer layers can be responsible for chromospheric and coronal heating (Stein 1967). Stochastic GWs, on the other hand, are expected to be generated in the early universe by hydrodynamic and hydromagnetic turbulence, as stated

*Email: Alberto.RoperPol@colorado.edu

in early papers by Kamionkowski et al. (1994) and Kosowsky et al. (2002). Recently the GW signal from turbulence has been studied in Niksa et al. (2018), and Saga et al. (2018); see also Caprini & Figueroa (2018) for a review, and references therein. It is therefore of interest to solve the GW equation simultaneously with the hydrodynamic or hydromagnetic equations for the turbulent sources driving these waves. Both hydromagnetic and GW equations are three-dimensional partial differential equations that can be solved with similar numerical techniques. However, the numerical properties are not quite equivalent and the physical intuition gained from numerical hydrodynamics gives insufficient guidance on the numerical requirements for the length of the timestep.

For the numerical solution of the fluid equations, usually no strong timestep constraint affects the accuracy of the solution. Therefore, in practice, one is able to use a timestep that is close to the stability limit of the scheme. However, with a finer timestep, more steps are needed to cover a given time span, so increased error accumulation is a possibility. The situation seems to be different for the solution of a wave equation sourced by hydrodynamic and hydromagnetic stresses. An accurate representation of the high wavenumber contributions hinges sensitively on the length of the timestep adopted. This leads to an artificial drop of the GW spectral energy density at high wavenumbers, due to the inaccuracy in the solution, if the timestep is not small enough.

In numerical hydrodynamics, the maximum permissible timestep δt is given by the CFL condition (Courant et al. 1928),

$$\delta t \leq C_{\rm CFL}\delta x/U_{\rm eff}, \tag{1}$$

where $C_{\rm CFL}$ is a number of the order of unity, δx is the mesh width, and $U_{\rm eff}$ is an effective propagation speed that could be the advection speed $\boldsymbol{u}$, the sound speed $c_{\rm s}$, the Alfvén speed $v_{\rm A}$ in the presence of magnetic fields, or, more generally, a combination of various relevant speeds such as $|\boldsymbol{u}|+(c_{\rm s}^2+v_{\rm A}^2)^{1/2}$.

A major difference between the hydrodynamic and wave equations lies in the fact that the former is nonlinear. Therefore, even though there may also be an inverse cascade, some energy always cascades down to smaller length scales. This does not happen with the GW equation. Here, instead, the high wavenumber contributions are only excited because they are being sourced at those high wavenumbers.

2. Basic equations

2.1. *Aeroacoustic and GW applications*

The aeroacoustic or Lighthill equation can be written in the form (Lighthill 1952, 1954)

$$\left(\frac{\partial^2}{\partial t^2}-c_{\rm s}^2\nabla^2\right)\rho'=\frac{\partial^2 T_{ij}}{\partial x_i\partial x_j}, \tag{2}$$

where $c_{\rm s}$ is the sound speed, ρ' is the density fluctuation, and $T_{ij}=\rho u_i u_j$ is the stress tensor with ρ being the density and $\boldsymbol{u}$ the turbulent velocity. It has also been applied to the sound generation from isotropic homogeneous turbulence (Proudman 1952). These authors found that the efficiency of sound production, i.e., the ratio between acoustic power and the rate of kinetic energy dissipation, $\epsilon\approx u_{\rm rms}^3/\ell$, scales with the Mach number ${\rm Ma}=u_{\rm rms}/c_{\rm s}$ to the fifth power. The intensity of sound waves is related to the fluctuations of the pressure field, which, in turn, is related to the density through the sound speed $c_{\rm s}$ as $p=\rho c_{\rm s}^2$ and is given by $I_{\rm r}=\left|\hat{p}^2\right|/(2\rho c_s)$. Based on Lighthill's analogy, the aeroacoustic theory describes the sources of sound waves in a multipole decomposition, where the intensity of the monopole contributions depends on the rate of energy flux ρu and is independent of the shape. The intensity of the dipole contributions scales as $I_r\propto u^6$ and the intensity of the quadrupole contributions as

$I_r \propto u^8$. Here r refers to the radial component in a local coordinate system around the source. This last result shows that the noise from free turbulence is very sensitive to the flow speed (Glegg & Devenport 2017).

The direct analogy between sound generation and GW generation from isotropic homogeneous turbulence has been exploited by Gogoberidze et al. (2007), Kahniashvili et al. (2008). In a universe with a stress-energy tensor having a relativistic equation of state (appropriate to the radiation-dominated epoch), using comoving spatial coordinates (which follow the expansion of the universe) and conformal time t (related to physical time $t_{\rm phys}$ through $\mathrm{d}t_{\rm phys} = a\mathrm{d}t$), the GW equation is given by

$$\left(\frac{\partial^2}{\partial t^2} - c^2\nabla^2\right) h_{ij}^{\rm TT} = \frac{16\pi G}{a^3 c^2} T_{ij}^{\rm TT}, \tag{3}$$

where a is the scale factor of the universe, $h_{ij}^{\rm TT}$ are the rescaled tensor-mode perturbations of the metric tensor related to physical metric tensor perturbations through $h_{ij}^{\rm TT} = a h_{ij}^{\rm TT,phys}$, c is the speed of light, and $T_{ij}^{\rm TT}$ is the transverse and traceless (TT) projection of the comoving stress-energy tensor T_{ij}; see Grishchuk (1974) and Deryagin et al. (1986). During radiation-dominated epoch, the scale factor a evolves linearly with conformal time, such that $a'' = 0$ and, hence, a damping term due to the expansion of the universe does not appear in equation (3). The TT projection can be computed in Fourier space (indicated by a tilde) as

$$\tilde{T}_{ij}^{\rm TT}(\boldsymbol{k},t) = (P_{il}P_{jm} - \tfrac{1}{2}P_{ij}P_{lm})\,\tilde{T}_{lm}(\boldsymbol{k},t), \tag{4}$$

where $P_{ij}(\boldsymbol{k}) = \delta_{ij} - \hat{k}_i\hat{k}_j$ is the projection operator, $\boldsymbol{k}$ is the wavevector, and $\hat{\boldsymbol{k}} = \boldsymbol{k}/k$ is its unit vector with $k = |\boldsymbol{k}|$ being the modulus. The total stress consists of the sum of Reynolds and Maxwell stresses, expressed for flat space-time geometry as

$$T_{ij} = (p/c^2 + \rho)\gamma^2 u_i u_j + p\delta_{ij} - B_i B_j/\mu_0 + \delta_{ij}\boldsymbol{B}^2/(2\mu_0) + ..., \tag{5}$$

where ρc^2 is now the radiation energy density, $\gamma = (1 - \boldsymbol{u}^2/c^2)^{-1/2}$ is the Lorentz factor, μ_0 is the vacuum permeability and the ellipsis denotes viscous and resistive contributions that are here ignored.

There is a striking analogy between the normalized radiation energy density ρ in the present context of an ultrarelativistic gas and the mass density in the usual hydromagnetic equations. This analogy was employed by Christensson et al. (2001) and Banerjee & Jedamzik (2004) to argue that the equations for the early universe could be solved using just ordinary hydromagnetic computer codes. Here and below, we expand γ in $\boldsymbol{u}/c$, i.e., $\gamma \sim 1 + u^2/c^2$, including only terms up to second order. We adopt Lorentz-Heaviside units for the magnetic field, so $\mu_0 = 1$. The p/c^2 term enters because in a relativistic plasma, the gas pressure is comparable to and equal to one third of the radiation energy density, ρc^2. Using the ultrarelativistic equation of state, we have $p = \rho c^2/3$, so the term in front of $u_i u_j$ reduces to $4\rho/3$. Hence, similar 4/3 factors appear in the hydromagnetic equations for an ultrarelativistic gas (Brandenburg et al. 1996, 2017, Kahniashvili et al. 2017), which are given by

$$\frac{\partial \ln\rho}{\partial t} = -\frac{4}{3}\left(\boldsymbol{\nabla}\cdot\boldsymbol{u} + \boldsymbol{u}\cdot\boldsymbol{\nabla}\ln\rho\right) + \frac{1}{\rho c^2}\left[\boldsymbol{u}\cdot(\boldsymbol{J}\times\boldsymbol{B}) + \eta\boldsymbol{J}^2\right], \tag{6}$$

$$\frac{\partial \boldsymbol{u}}{\partial t} = -\boldsymbol{u}\cdot\boldsymbol{\nabla}\boldsymbol{u} + \frac{\boldsymbol{u}}{3}\left(\boldsymbol{\nabla}\cdot\boldsymbol{u} + \boldsymbol{u}\cdot\boldsymbol{\nabla}\ln\rho\right) - \frac{\boldsymbol{u}}{\rho c^2}\left[\boldsymbol{u}\cdot(\boldsymbol{J}\times\boldsymbol{B}) + \eta\boldsymbol{J}^2\right] - \frac{c^2}{4}\boldsymbol{\nabla}\ln\rho + \frac{3}{4\rho}\boldsymbol{J}\times\boldsymbol{B} + \frac{2}{\rho}\boldsymbol{\nabla}\cdot(\rho\nu\boldsymbol{\mathsf{S}}), \tag{7}$$

$$\frac{\partial \boldsymbol{B}}{\partial t} = \nabla\times(\boldsymbol{u}\times\boldsymbol{B} - \eta\boldsymbol{J}), \tag{8}$$

where $\mathsf{S}_{ij} = \frac{1}{2}(u_{i,j} + u_{j,i}) - \frac{1}{3}\delta_{ij}\boldsymbol{\nabla}\cdot\boldsymbol{u}$ are the components of the rate-of-strain tensor with commas denoting partial derivatives, ν is the viscosity, and η is the magnetic diffusivity. We emphasize that all variables have been scaled appropriately so that terms proportional to $\dot{a}/a$ appear neither in equations (6)–(8) nor in equation (3). Nevertheless, there remains the $1/a^3$ term on the right-hand side of equation (3), which means that the source of GWs gradually declines.

Returning to the proposal of Christensson et al. (2001) and Banerjee & Jedamzik (2004) to use just ordinary hydromagnetic computer codes for simulating the early universe, it is useful to compare with the non-relativistic limit. Assuming $p \ll \rho c^2/3$, equations (6) and (7) reduce to

$$\frac{\partial \ln\rho}{\partial t} = -\boldsymbol{\nabla}\cdot\boldsymbol{u}, \tag{9}$$

$$\frac{\partial \boldsymbol{u}}{\partial t} = -\boldsymbol{u}\cdot\boldsymbol{\nabla}\boldsymbol{u} - \frac{1}{\rho}\boldsymbol{\nabla}p + \frac{1}{\rho}\boldsymbol{J}\times\boldsymbol{B} + \frac{2}{\rho}\boldsymbol{\nabla}\cdot(\rho\nu\mathsf{S}), \tag{10}$$

where an isothermal equation of state with $p = \rho c_{\rm s}^2$ is used (Christensson et al. 2001, Banerjee & Jedamzik 2004), and equation (8) is unchanged. However, in this paper we do not use the simplified equations even though the difference in the final results between the two sets of equations is small: the kinetic energy is less by a factor 4/3 in the relativistic case in the magnetically dominated case, while in the magnetically subdominant case, the magnetic energy is larger by a factor 4/3; see Brandenburg et al. (2017).

The six components of the spatial part of the symmetric tensor characterizing the linearized evolution of the tensor-mode metric perturbations h_{ij} contain four degrees of gauge freedom. In the TT gauge, these are eliminated by requiring $h_{ii}^{\rm TT} = 0$ and $h_{ij,j}^{\rm TT} = 0$, leaving only two components which, in the linear polarization basis, are the + and × polarizations. However, the projection onto that basis is computationally expensive, because it requires nonlocal operations involving Fourier transformations. It is therefore advantageous to evolve instead the tensor-mode perturbations of the metric tensor, h_{ij}, in an arbitrary gauge, compute $h_{ij}^{\rm TT}$ in the TT gauge, and then perform the decomposition into the linear polarization basis whenever we compute diagnostic quantities such as averages or spectra. Thus, we solve the linearized GW equation in the form

$$\left(\frac{\partial^2}{\partial t^2} - c^2\nabla^2\right) h_{ij} = \frac{16\pi G}{a^3 c^2} T_{ij} \tag{11}$$

for the six components $1 \le i \le j \le 3$. We emphasize that equation (11) is valid in the radiation-dominated epoch, where the scale factor increases linearly with conformal time. In the matter-dominate epoch, by contrast, there would be an additional damping term that is not relevant for our purpose. For test purposes, equation (11) can also be applied to a non-expanding universe by putting $a = 1$. It is therefore convenient to set $a = (t/t_*)^m$, where $m = 1$ for the radiation-dominated epoch and $m = 0$ in the case of a non-expanding universe. This case can be useful for comparisons with certain analytic solutions.

We use the Pencil Code for the numerical treatment of equation (11) together with equations (6)–(8). In its default configuration, it uses a sixth-order accurate discretization in space and a third-order accurate timestepping scheme.

2.2. *The TT projection*

To compute the physically observable tensor-mode metric perturbations, the GW energy density, as well as the degree of circular polarization (the physical observables of interest), we compute $h_{ij}^{\rm TT}$ and $\dot{h}_{ij}^{\rm TT}$ and express them in terms of the linear polarization basis. To compute

$h_{ij}^{\rm TT}$ from h_{ij}, we Fourier transform the six components of h_{ij} using the convention

$$\tilde{h}_{ij}(\boldsymbol{k},t) = \int h_{ij}(\boldsymbol{x},t)\, e^{-{\rm i}\boldsymbol{k}\cdot\boldsymbol{x}} d^3x, \tag{12}$$

for $1 \le i \le j \le 3$ and compute the components in the TT gauge as

$$\tilde{h}_{ij}^{\rm TT}(\boldsymbol{k},t) = (P_{il}P_{jm} - \tfrac{1}{2}P_{ij}P_{lm})\, \tilde{h}_{lm}(\boldsymbol{k},t). \tag{13}$$

Next, we compute the linear polarization basis,

$$e_{ij}^{+} = e_i^1 e_j^1 - e_i^2 e_j^2, \quad e_{ij}^{\times} = e_i^1 e_j^2 + e_i^2 e_j^1, \tag{14}$$

where $\boldsymbol{e}^1$ and $\boldsymbol{e}^2$ are unit vectors perpendicular to $\boldsymbol{k}$ and perpendicular to each other. Thus,

$$\tilde{h}^{+}(\boldsymbol{k},t) = \tfrac{1}{2}e_{ij}^{+}(\boldsymbol{k})\, \tilde{h}_{ij}(\boldsymbol{k},t), \quad \tilde{h}^{\times}(\boldsymbol{k},t) = \tfrac{1}{2}e_{ij}^{\times}(\boldsymbol{k})\, \tilde{h}_{ij}(\boldsymbol{k},t). \tag{15}$$

We then return into real space and compute

$$h^{+/\times}(\boldsymbol{x},t) = \frac{1}{(2\pi)^3} \int \tilde{h}^{+/\times}(\boldsymbol{k},t)\, e^{{\rm i}\boldsymbol{k}\cdot\boldsymbol{x}}\, d^3k. \tag{16}$$

Analogous calculations are performed for $\dot{h}^{+/\times}(\boldsymbol{x},t)$, which are used to compute the GW energy density.

2.3. *Linear polarization basis*

The linear polarization basis is formed by $\boldsymbol{e}^1$, $\boldsymbol{e}^2$ and $\boldsymbol{e}^3 = \hat{\boldsymbol{k}}$. To construct $\boldsymbol{e}^1$ and $\boldsymbol{e}^2$ from $\boldsymbol{k}$, we distinguish three cases

$$\text{for } |k_1| < \min(|k_2|,|k_3|): \quad \boldsymbol{e}^1 = \mathrm{sgn}(\boldsymbol{k})\,(0,-k_3,k_2), \quad \boldsymbol{e}^2 = (k_2^2+k_3^2,-k_1k_2,-k_1k_3), \tag{17}$$

$$\text{for } |k_2| < \min(|k_3|,|k_1|): \quad \boldsymbol{e}^1 = \mathrm{sgn}(\boldsymbol{k})\,(k_3,0,-k_1), \quad \boldsymbol{e}^2 = (-k_2k_1,k_3^2+k_1^2,-k_2k_3), \tag{18}$$

$$\text{for } |k_3| \le \min(|k_1|,|k_2|): \quad \boldsymbol{e}^1 = \mathrm{sgn}(\boldsymbol{k})\,(-k_2,k_1,0), \quad \boldsymbol{e}^2 = (-k_3k_1,-k_3k_2,k_1^2+k_2^2), \tag{19}$$

where we define the sign of a general wavevector $\boldsymbol{k} = (k_1,k_2,k_3)$ in the following arbitrary way

$$\mathrm{sgn}(\boldsymbol{k}) = \begin{cases} \mathrm{sgn}(k_3) \text{ if } k_3 \neq 0, \\ \mathrm{sgn}(k_2) \text{ if } k_3 = 0 \quad \text{and} \quad k_2 \neq 0, \\ \mathrm{sgn}(k_1) \text{ if } k_2 = k_3 = 0, \end{cases} \tag{20}$$

such that half of the wavevectors are considered positive and the other corresponding half of the wavevectors are considered negative. The way to choose which half of the wavevectors are positive is arbitrary and could be changed leading to the same result.

Note that neither $\boldsymbol{e}^1$ nor $\boldsymbol{e}^2$ flip sign under $\boldsymbol{k} \to -\boldsymbol{k}$. The reason for the $\mathrm{sgn}(\boldsymbol{k})$ term is the following. The linear polarization modes e_{ij}^{+} and $e_{ij}^{\times}$ must be even operators with respect to $\boldsymbol{k}$ to reproduce the required modes, as will be shown in next section with a simple one-dimensional Beltrami field example.

3. Results

3.1. *GWs for a Beltrami field*

It is useful to have an analytic solution to compare the numerical solutions against. A simple such example that has not previously been discussed in this context is the case of GWs

generated by a 1D magnetic Beltrami field in a non-expanding flat universe ($a = 1$),

$$\boldsymbol{B}(x) = B_0 \begin{pmatrix} 0 \\ \sin k_0 x \\ \cos k_0 x \end{pmatrix}. \tag{21}$$

where k_0 is the characteristic wavenumber of the Beltrami field.

The magnetic energy density is $\mathcal{E}_{\rm M} = B_0^2/2$, where B_0 is the amplitude of the Beltrami field. The Beltrami field can equally well be applied to the velocity field, i.e., $\boldsymbol{u}(x) = u_0 \left(0, \sin k_0 x, \cos k_0 x\right)^{\rm T}$, where the kinetic energy density is $\mathcal{E}_{\rm K} = \rho u_0^2/2$ and u_0 is the amplitude of the Beltrami field.

The fractional helicity of the magnetic field is ± 1 and has the same sign as the characteristic wavenumber k_0. The Beltrami field (when applied to $\boldsymbol{B}$) is force-free ($\boldsymbol{J} \times \boldsymbol{B} = \boldsymbol{0}$), so no velocity will be generated. We can therefore treat this magnetic field as given and do not need to evolve it. Writing the stress tensor as $T_{ij}(x) = -B_i B_j + \frac{1}{2}\delta_{ij}\boldsymbol{B}^2$ for $i, j = 2, 3$ and $T_{ij} = 0$ for $i = 1$ and/or $j = 1$, we have

$$T_{ij}(x) = \mathcal{E}_{\rm M} \begin{pmatrix} 0 & 0 & 0 \\ 0 & \cos 2k_0 x & -\sin 2k_0 x \\ 0 & -\sin 2k_0 x & -\cos 2k_0 x \end{pmatrix}. \tag{22}$$

For kinetic motions, the stress-energy tensor can be written as $T_{ij}(x) = \left(4\gamma^2 u_i u_j/c^2 + \delta_{ij}\right)\rho c^2/3$, for $i, j = 2, 3$ and $T_{ij} = 0$ for $i = 1$ and/or $j = 1$. Assuming constant ρ, after transverse projection constant terms do not affect the generation of gravitational waves. Hence, δ_{ij} terms can be neglected since it will be projected out and, in the same way, we can simplify terms $\sin^2 k_0 x$ and $\cos^2 k_0 x$ in the same sense. After neglecting constant terms, the stress-energy tensor for kinetic motions is

$$T_{ij}(x) = \frac{4}{3}\mathcal{E}_{\rm K}\left(1 + u_0^2/c^2\right) \begin{pmatrix} 0 & 0 & 0 \\ 0 & -\cos 2k_0 x & \sin 2k_0 x \\ 0 & \sin 2k_0 x & \cos 2k_0 x \end{pmatrix}, \tag{23}$$

which is equivalent to equation (22), with a different prefactor and opposite sign. From now on, we only refer to magnetic fields. However, all the computations and conclusions are analogously applied to kinetic motions.

Note that T_{ij} is automatically transverse and traceless, so $T_{ij} = T_{ij}^{\rm TT}$, and we can directly compute the $+$ and $\times$ components as

$$T^{+} = \mathcal{E}_{\rm M} \cos 2k_0 x, \quad T^{\times} = -\mathcal{E}_{\rm M} \sin 2k_0 x. \tag{24}$$

Assuming $h^{+} = h^{\times} = \dot{h}^{+} = \dot{h}^{\times} = 0$ at the initial time $t_0 = 0$, the time-dependent part of the solutions to equation (11) is proportional to $1 - \cos 2\omega_0 t = 2\sin^2 \omega_0 t$, where $\omega_0 = c k_0$, so we have

$$h^{+}(x,t) = \frac{8\pi G}{c^4 k_0^2}\,\mathcal{E}_{\rm M} \cos 2k_0 x\, \sin^2 \omega_0 t, \quad h^{\times}(x,t) = -\frac{8\pi G}{c^4 k_0^2}\,\mathcal{E}_{\rm M} \sin 2k_0 x\, \sin^2 \omega_0 t. \tag{25}$$

Using $h_{\rm rms}^2 = \langle h_{+}^2 \rangle + \langle h_{\times}^2 \rangle$, where $\langle \cdots \rangle$ refers to a volume average in physical space, we have

$$h_{\rm rms}(t) = \frac{8\pi G}{c^4 k_0^2}\,\mathcal{E}_{\rm M} \sin^2 \omega_0 t. \tag{26}$$

The GW energy density, $\mathcal{E}_{\rm GW}$, which is proportional to

$$\langle \dot{h}_{+}^2 \rangle + \langle \dot{h}_{\times}^2 \rangle = \left(\frac{8\pi G}{c^3 k_0^2}\right)^2 \mathcal{E}_{\rm M}^2 \sin^2 2\omega_0 t, \tag{27}$$

is given by

$$\mathcal{E}_{\rm GW}(t) = \frac{c^2}{32\pi G}\left(\langle \dot{h}_+^2\rangle + \langle \dot{h}_\times^2\rangle\right) = \frac{2\pi G}{c^4 k_0^2}\mathcal{E}_{\rm M}^2 \sin^2 2\omega_0 t. \tag{28}$$

The time-averaged values of $h_{\rm rms}$ and $\mathcal{E}_{\rm GW}$ are given by

$$h_{\rm rms} = \frac{4\pi G}{c^4 k_0^2}\,\mathcal{E}_{\rm M}, \quad \mathcal{E}_{\rm GW} = \frac{\pi G}{c^4 k_0^2}\,\mathcal{E}_{\rm M}^2. \tag{29}$$

Note that the energy ratio obeys $\mathcal{E}_{\rm GW}/\mathcal{E}_{\rm M} = h_{\rm rms}/4$ and is thus independent of k_0. The antisymmetric spectral function of the GWs is given in Fourier space by

$$\mathcal{H}_{\rm GW}(t) = \frac{c^2}{32\pi G} 2 \int_{4\pi} \tilde{h}^+ \tilde{h}^\times k^2 \,{\rm d}\Omega_k = \frac{\pi G}{c^4 k_0^2}\mathcal{E}_{\rm M}^2 \left(\sin^2 2\omega_0 t\right) \langle \delta_{2k_0} + \delta_{-2k_0}\rangle\,, \tag{30}$$

where ${\rm d}\Omega_k$ is the differential over the spherical surface. δ_{k_0} is the Dirac delta function, defined such that $\delta_{k_0}(k) = 1$ if $k = k_0$ and zero otherwise. The circular degree of polarization is obtained as the fraction of antisymmetric spectral function to GW energy density.

$$\mathcal{P}_{\rm GW} = \frac{\mathcal{H}_{\rm GW}}{\mathcal{E}_{\rm GW}} = \delta_{2k_0} - \delta_{-2k_0}, \tag{31}$$

such that the polarization degree of Beltrami fields is ± 1 and the sign is the same as the sign of the magnetic helicity.

3.2. *Numerical solutions at finite spatio-temporal resolution*

At small enough grid spacings and small enough timesteps, our numerical solutions reproduce the considered 1D Beltrami field assumed, according to equations (26) and (28) for small values of k. At coarser resolution, however, we find that $h_{\rm rms}(t)$ and $\mathcal{E}_{\rm GW}(t)$ are characterized by an additional decay of the form

$$h_{\rm rms}(t) = \left(8\pi G/c^4 k_0^2\right) \mathcal{E}_{\rm M} \sin^2(2\omega_0 t) e^{-\lambda t}, \quad \mathcal{E}_{\rm GW}(t) = \left(2\pi G/c^4 k_0^2\right)\ \mathcal{E}_{\rm M}^2 \sin^2(2\omega_0 t) e^{-\lambda t}, \tag{32}$$

where λ quantifies the numerical error in terms of the decay rate. We emphasize that $\lambda \neq 0$ is entirely artificial and has to do with imperfect numerics. Results for λ are given in table 1 as functions of δt (quantified by the Courant number $\delta t\, c/\delta x$) and GW wavenumber $k_{\rm GW}$ (normalized by $k_{\rm GW}/k_{\rm Ny} = k_{\rm GW}\delta x/\pi$), defined as

$$k_{\rm GW}^{-1}(t) = \int_0^\infty k^{-1} E_{\rm GW}(k,t) dk \Big/ \int_0^\infty E_{\rm GW}(k,t) dk. \tag{33}$$

We recall that k_0 is the wavenumber of the magnetic field, so $2k_0 = k_{\rm GW}$ is the wavenumber of the GWs generated by the 1D Beltrami field. We see from table 1 that the decay is largest close to $k_{\rm GW}/k_{\rm Ny}$ and varies between 6×10^{-2} (for $\delta t\, c/\delta x = 0.2$) and 10^{-3} (for $\delta t\, c/\delta x = 0.05$), for $k_{\rm GW}/k_{\rm Ny} = 1$. In figure 1 we plot contours of λ (color-coded) versus $k_{\rm GW}$ and δt. The largest values of λ occur when $k_{\rm GW} = k_{\rm Ny}$ and δt is large. We also see that the lines of constant decay rate scale like $\delta t \propto k_{\rm GW}^{4/3}$. In figure 2 we show λ separately versus $k_{\rm GW}$ and δt. We see that $\lambda \propto k_{\rm GW}^4$ and $\lambda \propto \delta t^3$, which explains the scaling seen in figure 1. The cubic scaling of λ with δt may be related to the third order accuracy of the timestepping scheme. The quartic scaling with $k_{\rm GW}$, on the other hand, is less obvious given that the spatial accuracy of the scheme is sixth order.

Table 1. Dependence of the decay rate of the numerical error λ on $k_{\rm GW}/k_{\rm Ny}$ and $\delta t\, c/\delta x$.

$\delta t\, c/\delta x$	$k_{\rm GW}/k_{\rm Ny}=1/4$	$1/2$	1
0.2	6.7×10^{-4}	1.0×10^{-2}	6.0×10^{-2}
0.1	8.2×10^{-5}	1.3×10^{-3}	8.0×10^{-3}
0.05	1.2×10^{-5}	3.2×10^{-4}	1.0×10^{-3}

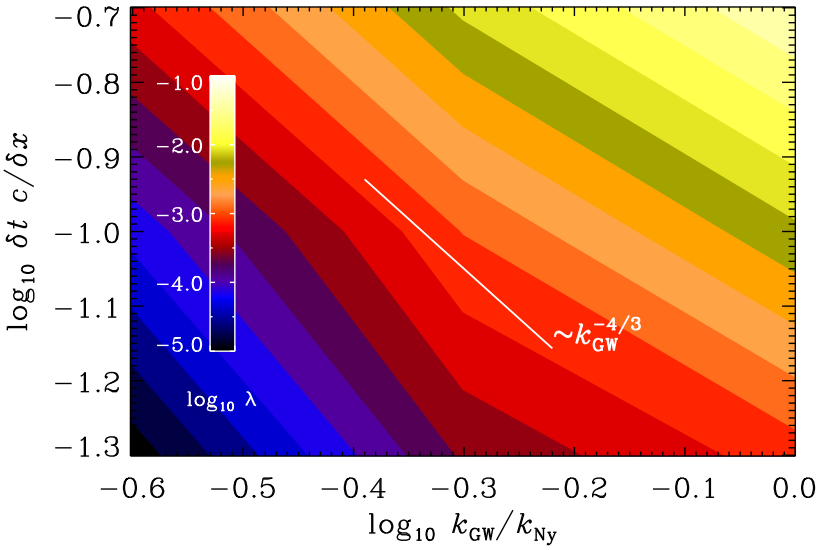

Figure 1. Dependence of the decay rate of the Beltrami field solution due to numerical error, λ, on $k_{\rm GW}/k_{\rm Ny}$ and $\delta t\, c/\delta x$. Blue (yellow) shades indicate low (high) numerical errors. The error is high when $k_{\rm GW}$ is close to the Nyquist wavenumber and δt is large. Slight departures from the expected power-law behavior (white line) can be attributed to measurement errors due to finite machine precision.

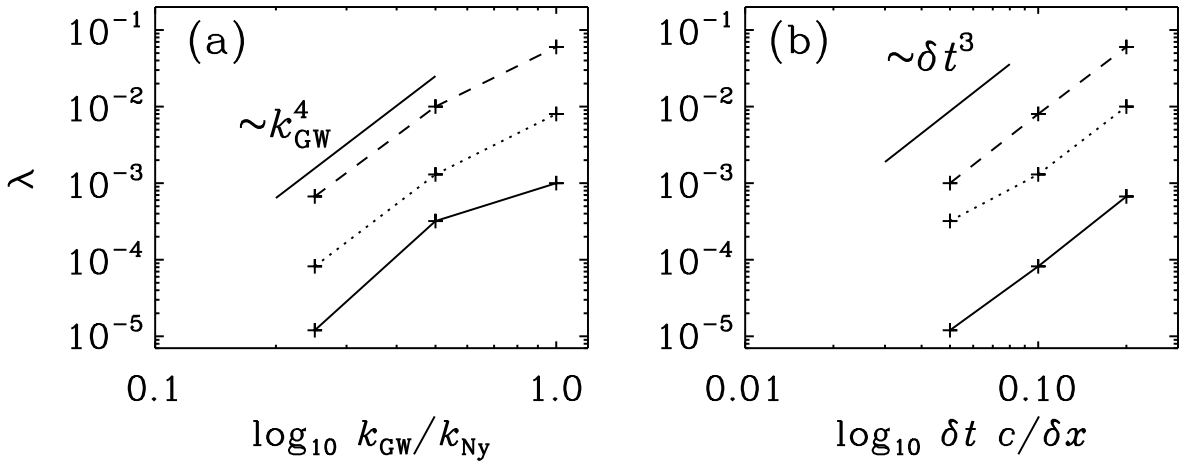

Figure 2. Scaling of the decay rate of the Beltrami field solution due to numerical error, λ, with $k_{\rm GW}/k_{\rm Ny}$ and $\delta t\, c/\delta x$. Again, departures from the expected power-law behavior (straight solid lines) can be attributed to finite machine precision.

3.3. *Timestep constraint in a turbulent case*

We now present an example where the timestep constraint becomes particularly apparent. As alluded to in the introduction, this is the case when GWs are being sourced by turbulent stresses. We consider here the case of decaying helical magnetic turbulence. This case was

Table 2. Dependence of the decay rate of the numerical error λ on $k_{\rm GW}/k_{\rm Ny}$ and $\delta t\,c/\delta x$ for hydromagnetically driven GWs. Dashes indicate that the decay rate was too small compared with the fluctuations and could not be determined.

$\delta t\,c/\delta x$	$k_{\rm GW}/k_{\rm Ny}=1/4$	1/2	1
0.23	0.012	0.16	1.1
0.12	–	0.015	0.12
0.05	–	–	0.006

originally considered in the cosmological context, using just an irregular magnetic field and no flows initially (Brandenburg et al. 1996, Christensson et al. 2001, Banerjee & Jedamzik 2004). Thus, the magnetic field is strong and the fluid motions are just the result of the Lorentz force. This leads to a generic situation in which the spectrum has a k^4 subinertial range spectrum (motivated by causality; see Durrer & Caprini 2003) and a k^{-2} weak turbulence spectrum at high wavenumbers (Brandenburg et al. 2015). Here, the magnetic energy spectrum $E_{\rm M}(k,t)$ is defined such that $\int E_{\rm M}(k,t)\,{\rm d}k=\mathcal{E}_{\rm M}(t)$. For an initial k^4 spectrum, the magnetic field undergoes inverse cascading such that the magnetic energy spectrum is self-similar and obeys

$$E_{\rm M}(k,t)=\phi_{\rm M}\left(k\xi_{\rm M}(t)\right), \tag{34}$$

where $\xi_{\rm M}(t)$ is the magnetic integral scale given by

$$\xi_{\rm M}(t)=\int_0^\infty k^{-1}E_{\rm M}(k,t)\,{\rm d}k\,\Big/\int_0^\infty E_{\rm M}(k,t)\,{\rm d}k. \tag{35}$$

In figure 3 we show for three times magnetic and GW energy spectra, $E_{\rm GW}(k,t)$, which are normalized analogously to $E_{\rm M}(k,t)$ such that $\int E_{\rm GW}(k,t)\,{\rm d}k=\mathcal{E}_{\rm GW}(t)$. Independent of the value of δt, the peak of $E_{\rm GW}(k,t)$ is seen to propagate gradually to smaller k. This is the inverse cascade owing to the presence of magnetic helicity (Pouquet et al. 1976, Biskamp and Müller 1999, Christensson et al. 2001). The ratio of $\mathcal{E}_{\rm M}/\mathcal{E}_{\rm GW}$ changes from about 100 at early times to about 20 at the last time as the magnetic field decays, while $\mathcal{E}_{\rm GW}$ stays approximately constant.

Let us now focus on the comparison of solutions for different timesteps. In figure 3 we show three solutions with $c\delta t/\delta x=0.23$, 0.12, and 0.05. While the magnetic energy spectra are virtually identical for different δt, even for high wavenumbers, the GW spectra is not. There is a dramatic loss of power at large k, when $c\delta t/\delta x=0.23$. A value of $c\delta t/\delta x=0.8$ is usually still safe as far as the hydrodynamics is concerned, but obviously not as far as the solution of GWs is concerned. This is a surprising result that may not have been noted previously.

To see whether the observed degradation is compatible with what has been seen for the monochromatic Beltrami field, we determine again the decay rates for three wavenumbers of the spectral GW amplitude. The result is given in table 2. We see that, although the scalings with $k_{\rm GW}$ and δt are compatible with what has been seen in section 3.2 for the Beltrami field, the actual values of λ are about 12 times larger. The reason for this is not clear at this point.

In addition to the numerical error discussed above, there is the possibility of a numerical instability that is distinct from the usual one invoked in connection with the CFL condition. This new instability emerges when the accuracy of the solution is already strongly affected by the length of the timestep, namely for $\delta t\,c/\delta x\gtrsim0.46$, which is still well within the range of what would normally (in hydrodynamics) be numerically stable. The problem appears at late times, after the GW spectrum has long been established. This new numerical error manifests itself as an exponential growth that is seen first at large wavenumbers and then at progressively smaller ones; see figure 4. Earlier studies showed that this problem cannot be controlled by adding explicit diffusion. Given that the solution is already no longer accurate for this length of the timestep, this numerical instability was not worth further investigation,

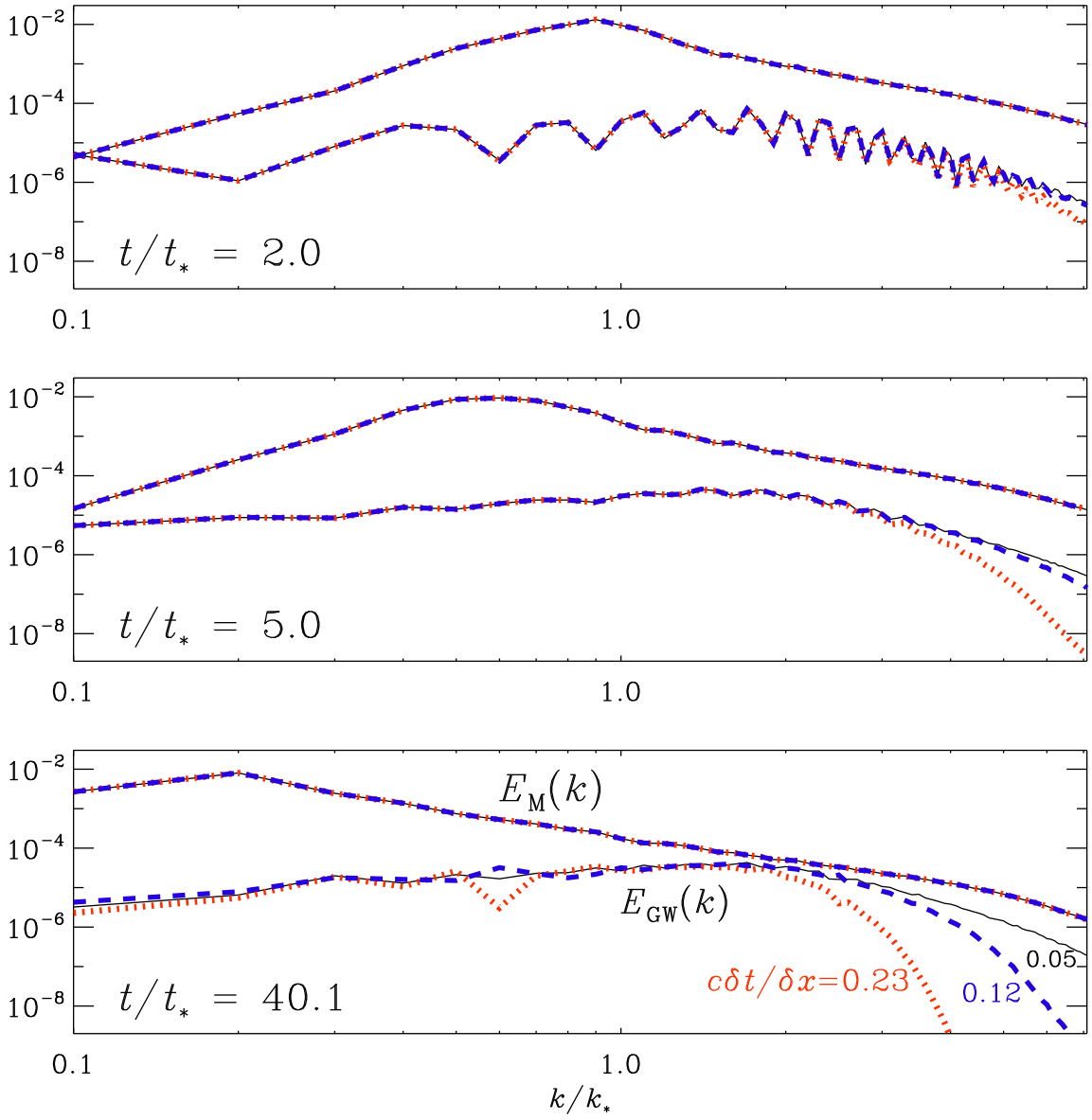

Figure 3. Gravitational wave (lower curves) and magnetic (upper curves) energy spectra at three different times, $t/t_* = 2$ (top panel), 5 (middle panel) and 40 (lower panel) where t_* is the conformal time at which the turbulence source turns on. Each panel shows three different timesteps: $c\delta t/\delta x = 0.23$ (red dotted lines), 0.12 (blue dashed lines), and 0.05 (black solid lines).

but it highlights once again the surprising differences in the numerical behavior of wave and fluid equations.

Looking again at the GW energy spectra at early times, we see wiggles in the spectrum. One might be concerned that these are caused by numerical artifacts, but the spatial distributions of h^+ and $h^\times$ look smooth; see figure 5. Thus, the wiggles in $E_{\rm GW}(k,t)$ are not artificial, but presumably related to the way the initial condition is posed using combined k^4 and k^{-2} power laws. They might appear as a transient effect in the evolution from the initially null GW energy density spectrum to the shape observed for later times. Indeed, at late times the wiggles disappear.

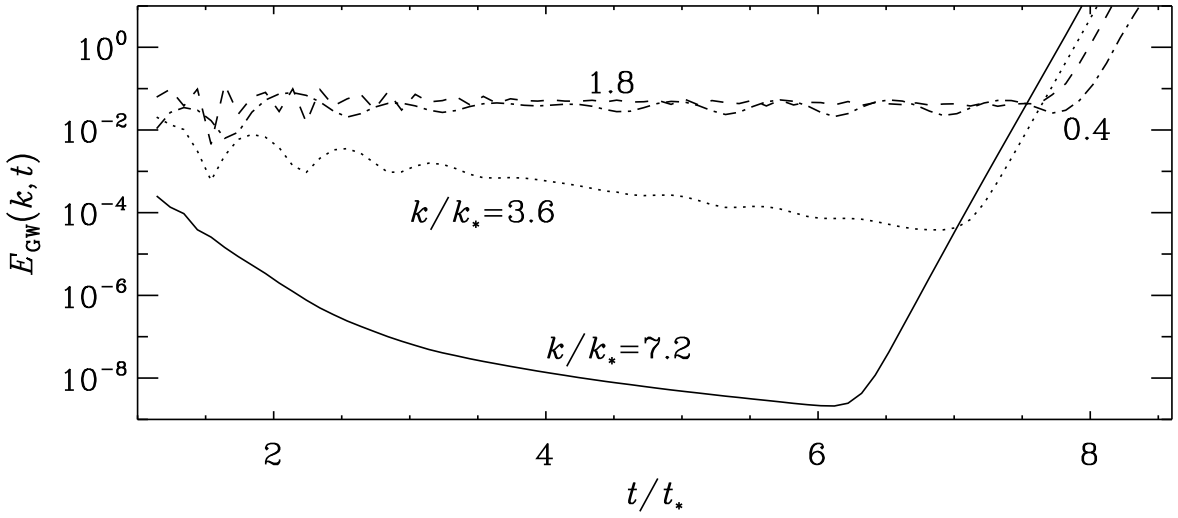

Figure 4. Late time numerical instability for $\delta t\, c/\delta x = 0.46$ seen in the temporal evolution of $E_{\rm GW}(k,t)$ after $t/t_* = 6$ for $k/k_* = 7.2$ (solid), 3.6 (dotted), 1.8 (dashed), and 0.4 (dash-dotted).

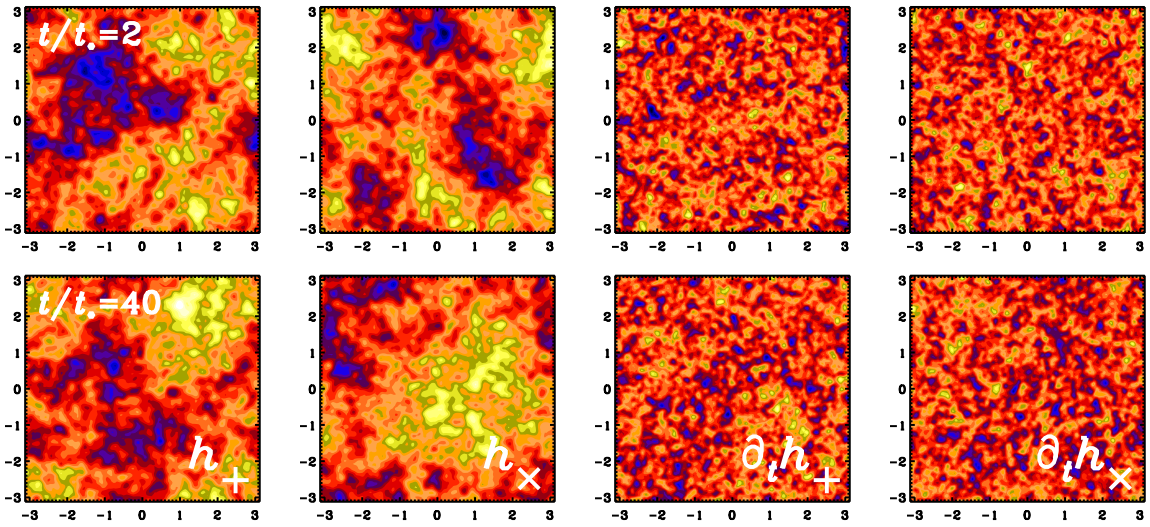

Figure 5. xy cross-sections through $z = 0$ of h_+, $h_\times$, $\partial_t h_+$, and $\partial_t h_\times$ at $t/t_* = 2$ (upper row) and $t/t_* = 40$ (lower row).

4. Can the timestep cause artifacts in hydrodynamic turbulence?

We have seen that hydromagnetic turbulence is not in any obvious way affected by the length of the timestep. However, there could be subtle effects. One such possibility is the bottleneck effect in hydrodynamic turbulence, which refers to a spectrum slightly shallower than the Kolmogorov $k^{-5/3}$ spectrum. This phenomenon is being explained by the inability of triad interactions with modes in the dissipative subrange to dispose of turbulent energy from the end of the inertial range (Falkovich 1994). This also has subtle effects on the growth rate of turbulent small-scale dynamos; see the recent paper by Brandenburg et al. (2018); hereafter referred to as BHLS.

In the simulations of BHLS, turbulence was being forced at low wavenumbers using an explicit forcing function $f(\boldsymbol{x},t)$ on the rhs of the momentum equation. It drives modes in a narrow band of wavenumbers. We consider here run D of BHLS, where driving was applied at

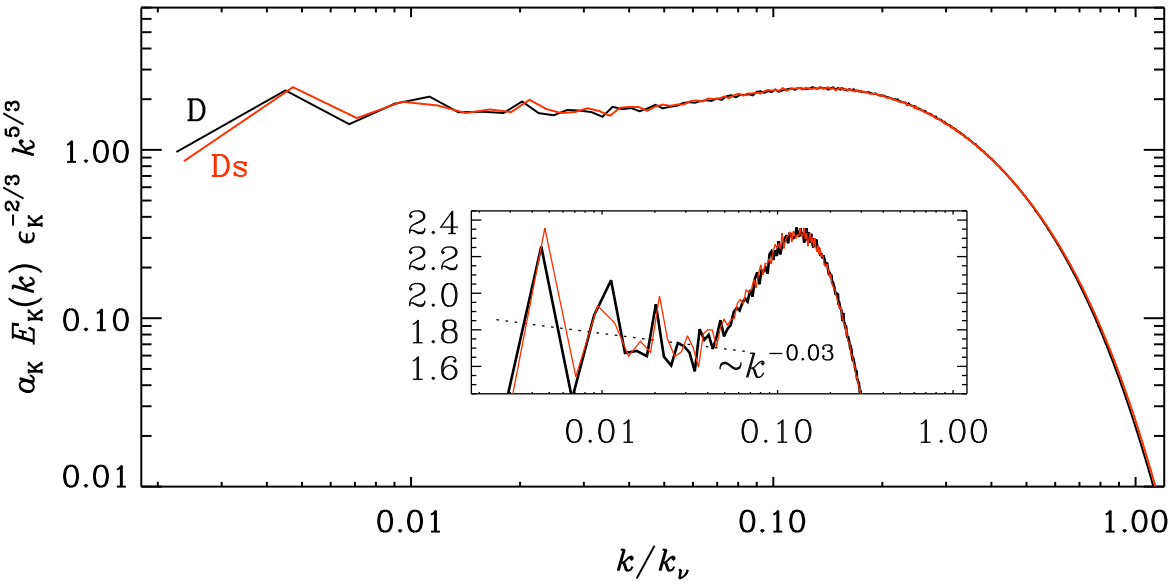

Figure 6. Comparison of compensated kinetic energy spectra for run D (black line) of BHLS with those of a continuation of this run with a four times shorter timestep (run Ds, red line). The inset shows the compensated spectra on a linear scale. The dotted line shows the theoretically expected inertial range correction proportional to $k^{-0.03}$.

wavenumbers between 1.4 and 1.8 times the lowest wavenumber of the domain, $k_{\rm min}=2\pi/L$ of a cubic domain of size L^3. The Reynolds number based on the average wavenumber was ≈ 1.5, but BHLS argued that the effective and relevant wavenumber for the smallest wavenumbers close to $k_{\rm min}$ is actually about twice as big and that the Reynolds number is therefore ≈ 200.

The important point of BHLS was to show that the bottleneck effect is independent of the forcing wavenumber, provided that the effective forcing wavenumber is used in the definition of the magnetic Reynolds number. Here we demonstrate that the bottleneck is not affected by the length of the timestep. The result is shown in figure 6, where we compare run D of BHLS with a new one called run Ds, where 's' indicates that that the timestep is shorter, such that now $\delta t\, c_{\rm s}/\delta x=0.15$.

It turns out that there is no difference in the energy spectrum relative to the usual case where the timestep obeys $\delta t\, c_{\rm s}/\delta x=0.60$. Thus, the artifacts reported in the present paper, namely the excessive damping of power at high wavenumbers, seems to be confined to the GW spectrum and does not affect in any obvious way the properties of the energy spectrum of hydromagnetic turbulence.

5. Conclusions

Our work has identified an important aspect that constrains the length of the timestep in numerical solutions of the linearized GW equation in a more stringent way than what is known in the more familiar hydrodynamic or hydromagnetic contexts. It affects the GW spectrum at high wavenumbers in a systematic way, which may have gone unnoticed in earlier investigations.

We argue that this numerical error is being masked in hydromagnetic turbulence by the fact that energy at high wavenumbers is constantly being supplied by a flux from larger scales. Thus, even though the amplitudes of velocity and magnetic fields are independent of the length of the timestep, the actual velocities (and especially their phases) may not be accurate. However, this numerical error does not seem to affect the energy spectrum, which could be primarily a consequence of a direct energy cascade. We therefore conclude that the direct

energy cascade is insensitive to numerical errors in hydrodynamic and hydromagnetic turbulence. A particularly interesting aspect of numerical solutions of turbulence is the bottleneck effect, i.e., a shallower fall-off of spectral energy just before turbulence disposes of its energy in the viscous dissipative subrange (Kaneda et al. 2003, Haugen & Brandenburg 2006, BHLS). One might therefore be concerned that this bottleneck itself could be the result of numerical artifacts. However, we have now shown that this is not the case and that the height of the bottleneck is independent of the length of the timestep.

The energy cascade argument does not apply to GW spectra, which obey linearized equations and are therefore not subject to a turbulent cascade. Therefore, we conclude that, to obtain the correct energy spectrum at high wavenumbers, it is essential to compute solutions with rather small timesteps of just a few percent of the CFL condition. This makes reasonably accurate GW spectra (where the decay rate is less than 1% of the Hubble rate, i.e., the case with $\delta t\, c/\delta x = 0.05$ in figure 3) by at least a factor of 10 more costly than what would naively be expected. It would be interesting to compare with spectral solvers in space and higher order timestepping procedures to see whether more economic schemes could be constructed.

Acknowledgements

This work was supported by National Science Foundation through the Astrophysics and Astronomy Grant Program (grants 1615100 & 1615940) and the University of Colorado through the George Ellery Hale visiting faculty appointment. Simulations presented in this work have been performed with computing resources provided by the Swedish National Allocations Committee at the Center for Parallel Computers at the Royal Institute of Technology in Stockholm. This work utilized the Summit supercomputer, which is supported by the National Science Foundation (award No. CNS-0821794), the University of Colorado Boulder, the University of Colorado Denver, and the National Center for Atmospheric Research.

References

Banerjee, R., Jedamzik, K., "Evolution of cosmic magnetic fields: From the very early Universe, to recombination, to the present," *Phys. Rev. D* **70**, 123003 (2004).

Biskamp, D., & Müller, W.-C., "Decay laws for three-dimensional magnetohydrodynamic turbulence," *Phys. Rev. Lett.* **83**, 2195–2198 (1999).

Brandenburg, A., Enqvist, K., & Olesen, P., "Large-scale magnetic fields from hydromagnetic turbulence in the very early universe," *Phys. Rev. D* **54**, 1291–1300 (1996).

Brandenburg, A., Haugen, N. E. L., Li, X.-Y., & Subramanian, K., "10.1093/mnras/sty1570," *Month. Not. Roy. Astron. Soc.* DOI:Varying the forcing scale in low Prandtl number dynamos (2018). (BHLS).

Brandenburg, A., Kahniashvili, T., Mandal, S., Roper Pol, A., Tevzadze, A. G., & Vachaspati, T., "Evolution of hydromagnetic turbulence from the electroweak phase transition," *Phys. Rev. D* **96**, 123528 (2017).

Brandenburg, A., Kahniashvili, T., & Tevzadze, A. G., "Nonhelical inverse transfer of a decaying turbulent magnetic field," *Phys. Rev. Lett.* **114**, 075001 (2015).

Caprini, C., Durrer, R., & Kahniashvili, T., "Cosmic microwave background and helical magnetic fields: The tensor mode," *Phys. Rev. D* **69**, 063006 (2004).

Caprini, C., Hindmarsh, M., Huber, S., Konstandin, T., Kozaczuk, J., Nardini, G., No, J. M., Petiteau, A., Schwaller, P., Servant, G., & Weir, D. J. , "Science with the space-based interferometer eLISA. II: gravitational waves from cosmological phase transitions," *J. Cosmol. Astropart. Phys.* **04**, 001 (2017).

Caprini, C., & Figueroa, D.: 2018, "Cosmological backgrounds of gravitational waves," arXiv:1801.04268

Christensson, M., Hindmarsh, M., & Brandenburg, A., "Inverse cascade in decaying 3D magnetohydrodynamic turbulence," *Phys. Rev. E* **64**, 056405 (2001).

Courant, R., Friedrichs, K., & Lewy, H., "Über die partiellen Differenzengleichungen der mathematischen Physik," *Mathematische Annalen,* **100**, 32–74 (1928); Engl. Transl.: On the partial difference equations of mathematical physics, *IBM J. Res. Dev.*, **11**, 215–234 (1967).

Deryagin, D. V., Grigoriev, D. Y., Rubakov, V. A., & Sazhin, M. V., "Possible anisotropic phases in the early universe and gravitational wave background," *Mod. Phys. Lett. A* **1**, 593–600 (1986).

Durrer, R., & Caprini, C., "Primordial magnetic fields and causality," *JCAP* **0311**, 010 (2003).

Falkovich, G., "Bottleneck phenomenon in developed turbulence," *Phys. Fluids* **6**, 1411–1414 (1994).

Galtier, S., Nazarenko, S., "Turbulence of weak gravitational waves in the early universe," *Phys. Rev. Lett.* **119**, 221101 (2017).

Glegg, S., & Devenport, W. *Aeroacoustics of low Mach number flows*. Elsevier (2017).

Gogoberidze, G., Kahniashvili, T., & Kosowsky, A., "Spectrum of gravitational radiation from primordial turbulence," *Phys. Rev. D* **76**, 083002 (2007).

Grishchuk, L. P., "Amplification of gravitational waves in an isotropic universe," *Sov. Phys. JETP* **40**, 409–415 (1974).

Grishchuk, L. P., "Amplification of gravitational waves in an isotropic universe," *Sov. Phys. JETP* **40**, 409–415 (1974).

Haugen, N. E. L., & Brandenburg, A., "Hydrodynamic and hydromagnetic energy spectra from large eddy simulations," *Phys. Fluids* **18**, 075106 (2006).

Kahniashvili, T., Brandenburg, A., Durrer, R., Tevzadze, A. G., & Yin, W., "Scale-invariant helical magnetic field evolution and the duration of inflation," *J. Cosmol. Astropart. Phys.* **12**, 002 (2017).

Kahniashvili, T., Gogoberidze, G., & Ratra, B., "Gravitational radiation from primordial helical magnetohydrodynamic turbulence," *Phys. Rev. Lett.* **100**, 231301 (2008).

Kamionkowski, M., Kosowsky, A., & Turner, M., "Gravitational radiation from first-order phase transitions," *Phys. Rev. D* **49**, 2837 (1994).

Kosowsky, A., Mack, A., & Kahniashvili, T., "Gravitational radiation from cosmological turbulence," *Phys. Rev. D* **66**, 024030 (2002).

Kaneda, Y., Ishihara, T., Yokokawa, M., Itakura, K., & Uno, A., "Energy dissipation rate and energy spectrum in high resolution direct numerical simulations of turbulence in a periodic box," *Phys. Fluids* **15**, L21–L24 (2003).

Lighthill, M. J., "On sound generated aerodynamically. I. General theory," *Proc. Roy. Soc. Lond. A* **211**, 564–587 (1952).

Lighthill, M. J., "On sound generated aerodynamically. II. Turbulence as a Source of Sound," *Proc. Roy. Soc. Lond. A* **222**, 1–32 (1952).

Niksa, P., Schlederer, M.,& Sigl, G.: 2018, "Gravitational waves produced by compressible MHD turbulence from cosmological phase transitions," arXiv:1803.02271

Pouquet, A., Frisch, U., & Léorat, J., "Strong MHD helical turbulence and the nonlinear dynamo effect," *J. Fluid Mech.* **77**, 321–354 (1976).

Proudman, I., "The generation of noise by isotropic turbulence," *Proc. Roy. Soc. Lond. A* **214**, 119–132 (1952).

Saga, S., Tashiro, H., & Yokoyama, S.: 2018, "Limits on primordial magnetic fields from direct detection experiments of gravitational wave background," arXiv:1807.00561

Stein, R. F., "Generation of acoustic and gravity waves by turbulence in an isothermal stratified atmosphere," *Solar Phys.* **2**, 385–432 (1967).